nature electronics

Article

https://doi.org/10.1038/s41928-024-01242-9

A microspectrometer with dual-signal spectral reconstruction

Received: 14 December 2023

Accepted: 12 August 2024

Published online: 17 September 2024

Check for updates

Xinchuan Du[1,4], Yang Wang[1,4], Yi Cui[1,4], Gaofeng Rao[1], Jianwen Huang[1], Xinrui Chen[1], Ting Zhou[1], Chunyang Wu[1], Zongyin Yang[2], Hanxiao Cui[3] ✉, Yicheng Zhao[1] ✉ & Jie Xiong[1]

Computational spectrometers with small footprints can be integrated with other devices for use in applications such as chemical analysis, medical diagnosis and environmental monitoring. However, their spectral resolution is limited because conventional photoelectric detectors only measure an amplitude-dependent response to incident light. Here we show that a deformable two-dimensional homojunction can be used to create a microspectrometer with dual-signal spectral reconstruction. The semifloating molybdenum disulfide homojunction exhibits a giant electrostriction effect through which the kinetics of photo-generated carriers can be manipulated via an in-plane electric field generated by gate voltage. By leveraging the tunability of both amplitude and relaxation time of the photoelectric response, a dual-signal response can be used with a deep neural network algorithm to reconstruct an incident spectrum. Our dual-signal microspectrometer has a footprint of 20 × 25 μm^2, offers a resolution of 1.2 nm and has a spectral waveband number of 380, which is comparable to benchtop spectrometers.

Optical spectroscopy is used for real-time analysis and non-destructive sampling in many fields, including material science, analytical chemistry and medical imaging[1–5]. Conventional spectrometers are based on the principles of optical dispersion and combine optical components to measure the intensity of each wavelength. Because the linear dimensions of these components determine the spectral resolution, they tend to be bulky. However, there is a demand for highly integrated, miniaturized spectrometers for use in applications that require portability, small sizes and low cost[6–11].

One strategy is to reconstruct the incident spectrum through matrix computation[12–14]. In this case, optical components are replaced by wavelength-sensitive photodetectors inside the spectrometer to achieve a small footprint and good integrability. Recent work has suggested that photodetector arrays on a compositionally graded nanowire can reduce the size of a spectrometer to 0.5 × 100 μm^2 with a resolution as high as 15 nm (ref. 15). Other approaches include engineering the electronic structure of black phosphorus to create an on-chip single-device spectrometer with a footprint and resolution of 9 × 16 μm^2 and 40 nm, respectively[16], and aligning the band structure of a WSe_2–MoS_2 van der Waals junction device (footprint of 8 × 22 μm^2)[17].

Despite the progress in miniaturized reconstructive spectrometers, their resolving performance does not match that of conventional dispersion-based spectrometers. The photodetectors produce an amplitude-dependent response to incident light, which is used to reconstruct the original spectra. The finite number of photodetector arrays or states leads to restricted dimensions for the wavelength-dependent response matrix that such spectrometers can produce[14–16]. Increasing the sampling depth of the photoelectric response can expand the matrix dimension, but there is substantial multicollinearity in the conventional response matrix that comprises only amplitude content (that is, photosensitivity) in the photoelectric response (Supplementary Note 1). The resolution could be improved

[1]State Key Laboratory of Electronic Thin Film and Integrated Devices, University of Electronic Science and Technology of China, Chengdu, China. [2]College of Information Science and Electronics Engineering, Zhejiang University, Hangzhou, China. [3]School of Aeronautics and Astronautics, Sichuan University, Chengdu, China. [4]These authors contributed equally: Xinchuan Du, Yang Wang, Yi Cui. ✉e-mail: hanxiao.cui@scu.edu.cn; zhaoyicheng@uestc.edu.cn

https://doi.org/10.1038/s41928-024-01242-9

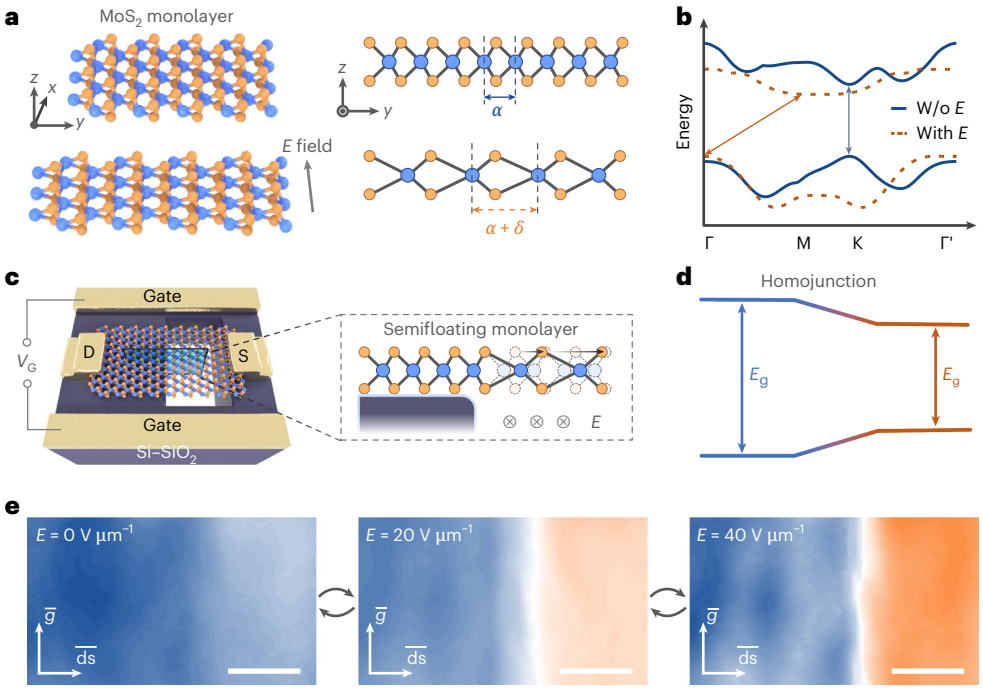

Fig. 1 | Architecture and property of the deformable 2D homojunction. **a**, Illustration of the in-plane electric field induces electrostriction (*E*) effect on monolayer MoS_2 (right), with a side view (right) showing the lattice deformation during this process. **b**, Comparison of the band structure (lowest conduction band and highest valence band) with and without (w/o) applying an electric field. **c**, Schematic of our deformable homojunction device with drain (D) and source (S) electrode at the two sides of MoS_2 (right). The cross-section shows that the in-plane electric field induces strain in the floating region of monolayer MoS_2 (left). **d**, Band structure schematic of the homojunction. **e**, Raman mappings of the MoS_2 E_{2g} peak at different electric field intensities. The field-induced lattice deformation can cause the bathochromic shift (blue to orange in mapping colour) of the E_{2g} peak at the floating region. $\bar{g}$ represents gate-gate orientation; $\overline{ds}$ represents drain-source orientation. Scale bar, 1 μm.

by including extra information that does not have a multicollinearity issue, such as relaxation time, to create an expanded response matrix (Supplementary Fig. 1).

In this Article, we report a photodetector-based reconstructive spectrometer with a footprint of 20 × 25 μm^2 based on a deformable semifloating two-dimensional (2D) homojunction with a tunable photoelectric response to both amplitude and relaxation time. The spectrometer contains a monolayer of molybdenum disulfide (MoS_2) transferred onto a substrate with a pre-etched vertical groove. The floating portion of the MoS_2 monolayer has a giant electrostriction effect that can tune the bandgap and carrier kinetics of the material. Thus, while typical photodetector-based reconstructive spectrometers modulate the amplitude response due to a bandgap change, this structure modulates the amplitude and relaxation time simultaneously. Using the dual-signal response from our miniaturized spectrometer, a deep neural network (DNN) algorithm can be trained to reconstruct incident spectra with a resolution of 1.2 nm and a waveband number of 380.

Deformable 2D homojunction with electrostriction effect

The floating MoS_2 monolayer exhibits a giant electrostriction effect under an in-plane electric field (Fig. 1a)[18,19]. Electrostriction-induced strain can reconfigure the MoS_2 electronic structure from a large direct bandgap to a small indirect bandgap, as confirmed by density functional theory simulations (Fig. 1b and Supplementary Fig. 2). The device is fabricated by transferring epitaxially grown MoS_2 monolayers to pre-etched U-groove regions on HfO_2–SiO_2 substrates (Fig. 1c). One pair of Cr–Au electrodes contacts the channel material on both sides of the U-groove as the source and/or drain electrodes, while the other pair is oriented perpendicular to the source–drain direction to supply in-plane electric fields (Supplementary Fig. 3). Notably, the electric field can induce lattice deformation in the floating region without effecting the non-floating area, owing to strong interactions between the substrate and the MoS_2 monolayer[20,21]. By applying an in-plane electric field, a tunable 2D homojunction can be created (Fig. 1d).

The asymmetric strain distribution in the semifloating 2D homojunction is confirmed by Raman mapping of the E_{2g} peak over the active monolayer on the U-groove region[22], where a steep strain gradience can be observed at the edge of the groove (Fig. 1e). The strain gradient, which is only strongly evident in the monolayer MoS_2, becomes more pronounced with an increasing electric field. Moreover, the spectrometer with double- or multi-layer MoS_2 shows negligible Raman E_{2g} peak shift and electric transport modulation under gate voltage (Supplementary Fig. 4). As supported by photoluminescence spectra, the strain also causes a noticeable change in the optical bandgap of the MoS_2 monolayer[23–25] (Supplementary Fig. 5). The peak position gradually shifts from approximately 690 nm in the non-floating region to 775 nm in the floating region as the in-plane electric field increases to its upper limit value of 60 V μm^{-1} (Supplementary Fig. 6). Notably, the strain and optical bandgap change are highly reversible over thousands of cycles (Supplementary Fig. 7), and the transport characteristics of the device show only a small variation (Supplementary Fig. 8), indicating the potential of our processing technology to expand towards large-scale array detectors.

Under an increasing electric field, the side view of the semifloating MoS_2 monolayer is illustrated in Fig. 2a. The corresponding energy band diagram would gradually evolve into a type-I homojunction, which is expected to cause gradual increment of the photoelectric response in the long wavelength range due to the bandgap reduction of the MoS_2 monolayer in the floating region (Fig. 2b). Further considering the inevitable defect states within the material, the strain gradient in the floating region would drive the accumulation of holes at the junction and reduce

https://doi.org/10.1038/s41928-024-01242-9

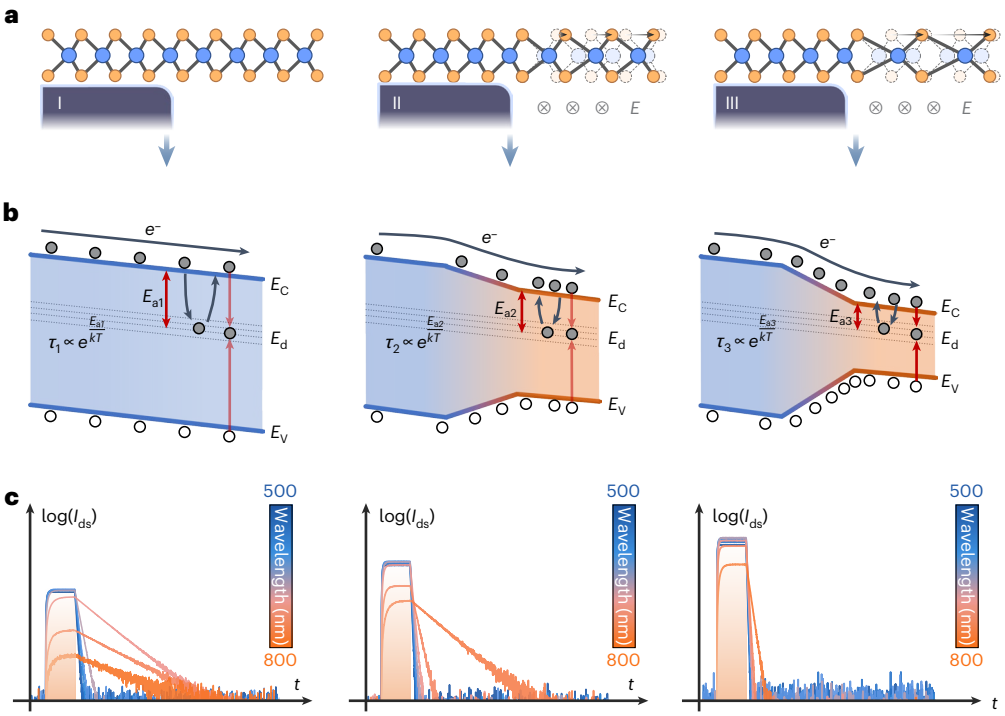

Fig. 2 | Photoelectric-response mechanism and characteristics of the gate-tunable 2D homojunction. a, Schematic of the homojunction device at initial state (left) and under in-plane electric field modulation (middle and right). **b**, Mechanistic diagram of spectral relaxation response regulation. The photoelectric relaxation time (τ) is dominated by the trapping and detrapping process of electrons (e^-) at energy levels of defect states. Particularly the energetic depth of the defect (E_a, equivalent to $E_C - E_d$) that affects the detrapping rate exponentially (left). With the reduction in bandgap, E_a is also reduced synchronously, making the relaxation time of photocarriers sensitive to electronic structure modulation (middle and right). **c**, Pulsed-light-induced transient current response. It is obtained by irradiating 20 ms monochromatic light pulses with various wavelengths at initial state (left) and serials in-plane electric field intensities (middle, 20 V μm^{-1}; right, 40 V μm^{-1}).

the activation energy for electrons detrapped from defect states, thus accelerating the decay process of photocarriers[26], as shown in the inset of Fig. 2b and Supplementary Note 2. This is verified by measuring the photoelectric response of the device under a series of pulsed-light illumination. Both the relaxation time and amplitude in the photoelectric response are effectively modulated by in-plane electric fields and are dependent on the wavelength of the monochromatic light (Fig. 2c). In the short-wavelength range with stronger electric fields, both the relaxation time and amplitude decrease. A continuous gradient of bandgaps spans from 1.8 to 1.6 eV, corresponding to a response cut-off extending from 700 to 800 nm. The relaxation time is dominated by the detrapping process or Shockley–Read–Hall recombination of photocarriers in deep-level defects in our device, which is manifested by the ultra-slow decay with first-order kinetics in the photocurrent response.

Dual-signal spectral reconstruction strategy

For any incident spectrum, our device can produce two distinct response signals, one is a photocurrent signal and one is a relaxation time signal. Under tunable gate voltage (V_G), the two signals form the basis for dual-signal spectral reconstruction, as indicated by $I(V_G)$ and $T(V_G)$ in Fig. 3a. To collect both relaxation time and photocurrent information as a function of monochromatic light wavelength under different gate voltages, we use chopped incident light through a mechanical chopper at a fixed frequency while scanning the in-plane gate voltages and extracting the photocurrent response signal through a transconductance amplifier, as illustrated in the equivalent circuit (Fig. 3b and Supplementary Fig. 9). The original photoelectric-response waveform is then converted to the photocurrent signal via an envelope discriminator. The chopper's reference signal with the photocurrent response signal is obtained by low-pass filtering and hysteresis comparison, in which the time delay (Δt) between the photoelectric-response waveform wave and the chopper's reference signal is extracted as the lumped relaxation time and further converted by a phase discriminator to the relaxation time signal. This method enables high-precision photocurrent and relaxation time measurement at a low temporal sampling frequency. We find that the wavelength-dependent response patterns of relaxation time and amplitude are distinct from each other within the detection range (Supplementary Fig. 10). Therefore, our device features an additional set of relaxation time dimensions in the response matrix compared to conventional photoelectric devices used for reconstructive spectrometers[15,16,27–31]. From a physical perspective, reconstructive spectrometers with tunable relaxation time are advantageous owing to their inherently different physical mechanism of tunability, highly sensitive response to external stimuli and synchronized signal collection with amplitude. These advantages are expected to increase the spectral resolution of such a reconstructive spectrometer while maintaining a similar operating speed and power consumption to conventional ones.

With the above dual response matrix, we can reconstruct the incident spectrum from a set of signals composed of relaxation time and amplitude under different gate voltages. In contrast to the conventional reconstruction process, this dual response matrix with relaxation time cannot be reduced analytically to a set of linear equations as functions of an unknown vector (Supplementary Note 3). Here, we develop a DNN with five hidden layers to learn the mapping relation between signal and original spectral vectors[32]. Several incident spectra, precalibrated by a commercial spectrometer, are used as target output and the response signals of the device at different electrical states are used as input to train the DNN for the spectral reconstruction (Fig. 3b).

The dual signals give rise to a better resolution for spectral reconstruction, compared to amplitude-only signals (Supplementary Note 1).

https://doi.org/10.1038/s41928-024-01242-9

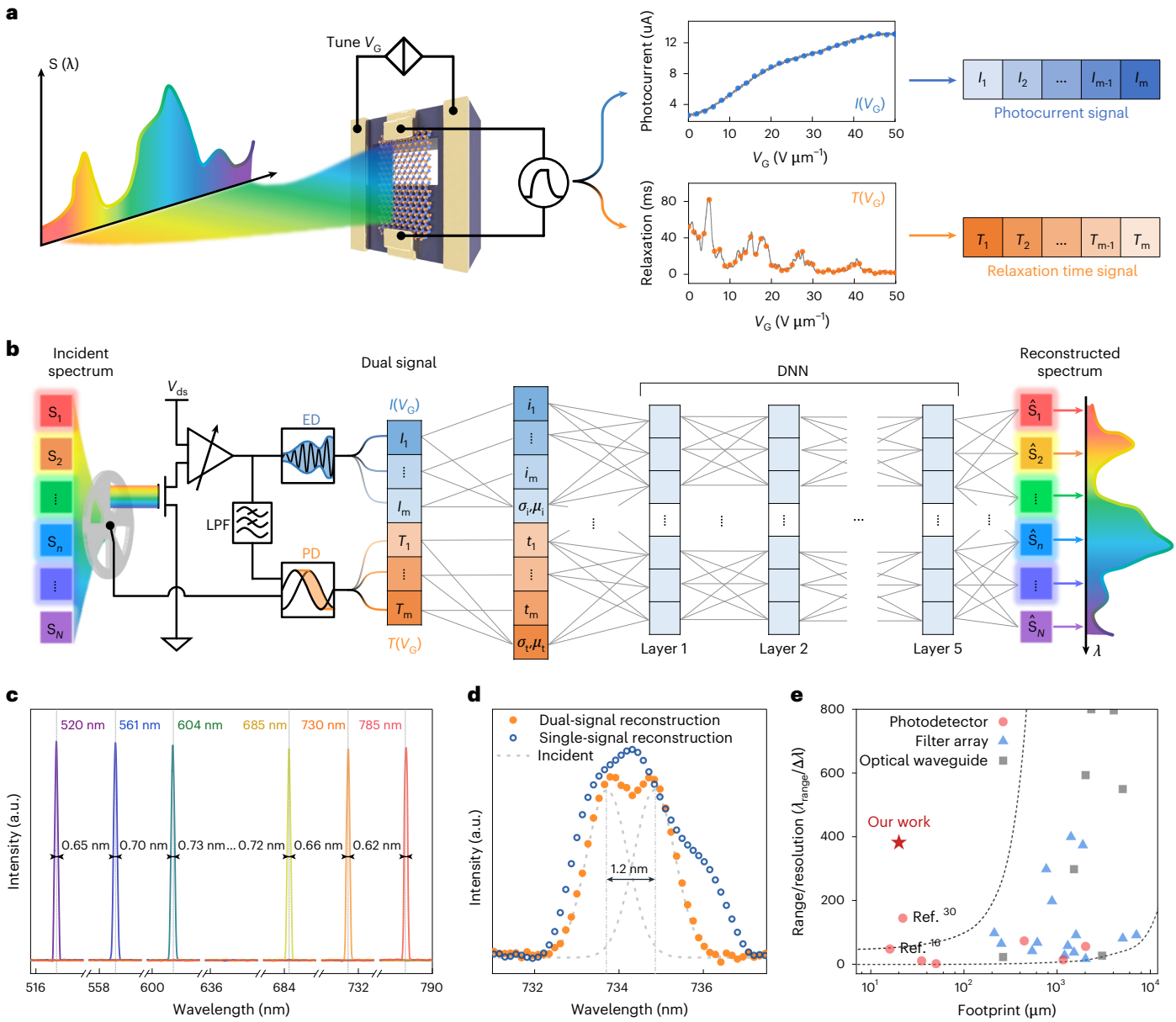

Fig. 3 | Dual-signal spectral reconstruction using the gate-tunable 2D homojunction. a, Dual-signal construction illustration. By adjusting the gate voltage (V_G) the photocurrent and relaxation time exhibit varying trends for the same incident spectrum (S), thereby yielding the dual signal. I_m and T_m are the raw photocurrent and relaxation time data, respectively. i_m and t_m are normalized data. μ_i/σ_i, σ_t/μ_t represent the mean/variance value of the normalized photocurrent and relaxation time. **b**, Dual-signal spectral reconstruction illustration. The incident light is directed onto the photosensitive region through a chopper. The dual signal is then detected separately by demodulating the transient photoelectric-response signal using a low-pass filter (LPF), envelope discriminator (ED) and phase discriminator (PD). The $I(V_G)$ and $T(V_G)$ are used as the input features of the trained DNN, and the network output is the reconstructed spectrum ($\hat{S}$). **c**, The reconstructed spectra of a range of monochromatic peaks and the corresponding full-width at half-maximum over the entire operational waveband. **d**, The dual- and single-signal reconstructed spectra of the dichromatic light with a 1.2 nm wavelength spacing. **e**, Spectral waveband number (defined as the ratio of operational waveband width to wavelength resolution) versus spectrometer footprint of reported reconstruction spectrometers.

For monochromatic light, the spectrometer can effectively reconstruct the spectra with a full-width at half-maximum of approximately 0.6 nm in the entire operating wavelength range (Fig. 3c). The resolution of the microspectrometer is slightly different at different wavebands from 450 to 800 nm. In addition, at the edge of the operation waveband (wavelength less than 450 nm and greater than 800 nm) the measurement of relaxation time and amplitude in photoelectric response are more susceptible to non-negligible errors owing to a lower signal-noise ratio, due to the attenuation of the specific detectivity (Supplementary Figs. 11 and 12). Considering the presence of multicollinearity features in the reconstruction process, this error could be further transmitted into the reconstruction results. For dichromatic light, the dual-signal reconstruction can clearly distinguish a difference of 1.2 nm in the peak position and shows a higher resolution than the single-signal reconstruction result (Fig. 3d). From Fig. 3e and Supplementary Fig. 13, it is found that the spectrometer with dual-signal response breaks the tradeoff between footprint and waveband number in previous spectrometers. The spectral resolving power is now comparable to that of conventional centimetre-scale spectrometers and even some benchtop spectrometers.

https://doi.org/10.1038/s41928-024-01242-9

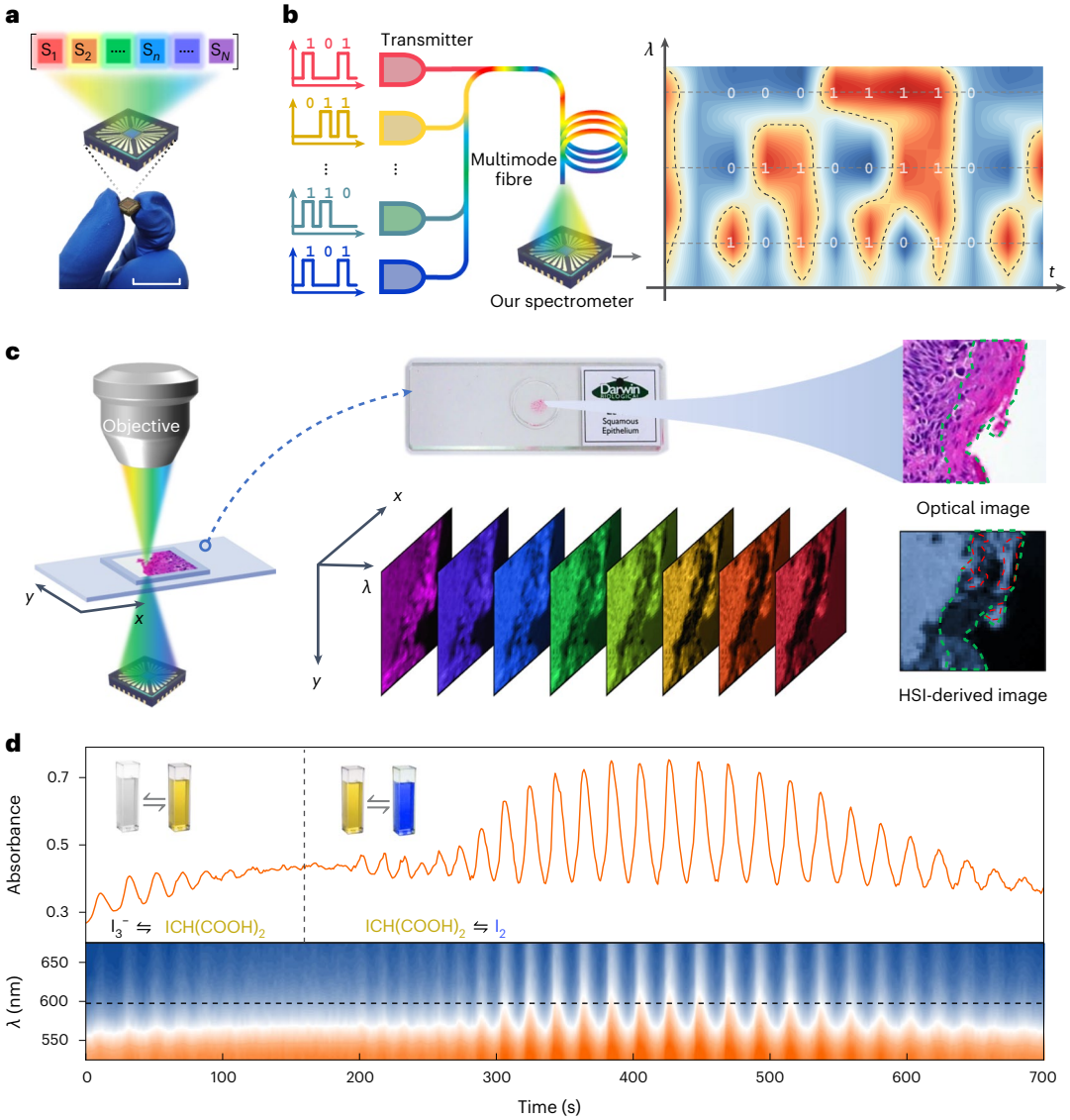

Fig. 4 | Practical applications of dual-signal spectral reconstruction. a, The incorporated spectrometer in a chip package. Scale bar, 10 mm. **b**, Wavelength-division multiplexing optical communication diagram. The transmitter consists of multiple independently modulated monochromatic light sources, and the mixed light is coupled into a multimode fibre. At the receiving end, our spectrometer acts as a demultiplexer for the wavelength-division multiplexing signals, to reconstruct the original modulation information. The right panel shows our decoupling result of three-waveband wavelength-division multiplexing signals continuous transmission parallel increasing binary. **c**, The bio-slice sample HSI measurements. We have transmission mapping the HSI of a squamous epithelium slide sample based on a translation stage and obtain the transmittance spatial distribution at different wavelengths. Compared to optical images, HSI allows for the observation of more pronounced subregions of contrast (red dashed area) in areas that are difficult to distinguish in optical image (green dashed area). **d**, The time-resolved absorbance spectra of iodine clock reaction solution. The profile tendency of absorbance at 597.5 nm is independently plotted on the upper panel. The I_3^- (colourless) and $ICH(COOH)_2$ (amber) first oscillate, and the solution gradually becomes blue as accumulative iodine (I_2) is coloured violet by starch. Last, the oscillation is gradually attenuated by the consumption of oxidant.

Practical applications of the spectrometer

Assembling the device into a chip package is promising for applications in various scenarios (Fig. 4a). The reliability of this microspectrometer, examined by more than 10,000 incident spectra, is exhibited by a low coefficient of variation of about 0.2% (Supplementary Fig. 14). Given a standard specimen of $KMnO_4$ solution and artificial mixed light, our reconstruction results are also highly consistent with commercial spectrometers (Supplementary Figs. 15 and 16). Such high reliability of spectral reconstruction opens opportunities in high-capacity optical communication systems with wavelength-division multiplexing. We use several independently modulated monochromatic light sources as the transmitter, coupling them into a multimode fibre via a beam combiner, and directing them onto the spectrometer to decode the original modulation information. By configuring the appropriate spectral sampling accuracy for the target bands, the acquisition time for each frame of spectra is reduced to 200 ms. Even in this high-speed spectral acquisition mode, the spectrometer retains precise resolution of spectral intensity and central wavelengths for various bands such as 660, 720 and 780 nm. This proficiency allows for accurate decoding of transmission spectral features, presenting the microspectrometer as a potentially effective decoder for an optical wavelength-division multiplexing network (Fig. 4b). The microspectrometer with large dynamic range can also be used in constructing a hyperspectral imaging (HSI) microscope that could have a large impact on bioinformatics (Supplementary Fig. 17). Here, we present the HSI of a squamous epithelium slide sample. By performing linear operations on the data

from different wavelengths in HSI, we obtain an HSI-derived image that contains more information than a metallurgical microscope (Fig. 4c). We further evaluate the spatial transmission spectra of a colour Alta, showing the capability of distinguishing subtle differences between colours that are indiscernible to the human eye (Supplementary Fig. 18). Besides its applications in communications and medical imaging, its fast spectral measurement is also helpful in tracking certain kinetics of chemical reactions, for instance, a classic oscillation chemical reaction (Fig. 4d). The time-resolved absorption spectra show the periodic changes in solutions with an iodine clock reaction.

Conclusions

We have reported a reconstructive microspectrometer with a footprint of $20 \times 25\ \mu m^2$, nanometre-level spectral resolution and a high waveband number by using a deformable 2D homojunction with a tunable photoelectric response. A high spectral resolution is achieved using a dual-signal spectral reconstruction method that leverages a feature of the photoelectric response of our homojunction, where the bandgap (amplitude) and carrier kinetics (relaxation time) can be tuned via an in-plane electric field due to the giant electrostriction effect in the floating MoS_2 monolayer. The advantage of this method lies in its dual sampling depth and reduces the multicollinearity of the response matrix. At the same time, the electrically tunable homojunction is compatible with large-scale hyperspectral array fabrication and integration. In the future, the wavelength range could be expanded from ultraviolet to infrared and the spectra resolution improved to sub-1 nm by combining various 2D semiconductors and modulation strategies. Such microspectrometers could help accelerate the development of advanced spectral imaging for portable devices, in situ characterization and lab-on-a-chip appliances.

Methods

Spectrometer fabrication

The preparation of vertical grooves in the SiO_2 layer of Si–SiO_2 substrates was achieved by reactive ion etching (RIE). Specifically, the target flake was selected, and the size of the available region of the MoS_2 nanoflakes was calibrated. Then the sizes and arrangements of the vertical grooves were customized on the basis of the calibrated region of the MoS_2 nanoflake. The customized pattern was then exposed to the substrate coated with AZ4620 (Microchemicals GmbH) photoresist (substrate baked at 200 °C for 10 min, cooled and spin-coated at 500 rpm for 10 s and 3,000 rpm for 30 s) by contact ultraviolet lithography. Next, the substrate was developed and baked at 120 °C for 5 min to remove water vapour from the surface and to allow the photoresist to bond more firmly to the substrate. In the RIE processing, the etching gas was a mixture of CHF_3 and CF_4 (8:1), and the etching gas flow rate was controlled at 10 sccm. The chamber pressure was controlled at 1×10^{-3} torr, and the etching power was set to 120 W. The etching rate of SiO_2 was about 23 nm min^{-1}, so the vertical grooves were ~460 nm deep after 20 min of etching. The substrate surface was cleaned with acetone, alcohol and isopropyl alcohol to remove the AZ4620 photoresist. Subsequently, a 5-nm-thick HfO_2 insulating layer was grown on the surface by atomic layer deposition. The CVD-grown MoS_2 nanoflakes were delicately transferred to the previously fabricated substrates by dry transfer. The detailed procedure was to first paste the polyvinyl alcohol (PVA) onto the target MoS_2 nanoflakes by polydimethylsiloxane (PDMS)-loaded PVA under a microscope. The substrate was then heated to tightly engage the PVA and the substrate, separating the PVA from the PDMS. After the substrate cooled, the PVA was carefully peeled off from the substrate. The PVA was then loaded onto a new slice of PDMS. We continued to finely align the MoS_2 nanoflakes on the PVA with the etched areas on the substrate on the transfer table (to ensure no mechanical breakage of the MoS_2 nanoflakes, the substrate must be prewarmed and the PVA kept in gentle contact with the substrate). The substrate was then stood in deionized water to remove the PVA. Next, the first electron-beam lithography (using polymethyl methacrylate photoresist) was performed, and RIE etching was applied to separate MoS_2 channel regions from the intact MoS_2 nanoflakes. The second electron-beam lithography was performed to fabricate customized electrode structures. After development, Cr, Au and Al electrodes (5, 50 and 2 nm) were prepared using thermal vapour deposition. Finally, aiming to make the high-voltage-driven electrodes less susceptible to vacuum breakdown caused by field emission, a 5-nm-thick layer of HfO_2 was grown on the surface of the Al_2O_3, which was formed by natural oxidation at ambient conditions.

Material characterization

The morphology of as-synthesized MoS_2 nanosheets was characterized by an OLYMPUS microscope and Hitachi E-sweep atomic force microscope. The vibration modes and of the MoS_2 were obtained from Raman spectra collected using a WITec Alpha 300 confocal Raman microscope with an excitation source of a continuous wave 532 nm laser. To avoid laser heating, which often results in broadening and shifting of the Raman peaks or damaging the sample, the laser power was adjusted to be as small as possible within the signal detection limit. Here, we used a laser power of about 8.6–1,000 μW for Raman imaging and photoluminescence.

Photoelectric measurement

The as-prepared spectrometer circuit system was connected to source measure units (Keithley 2604B) through the rear interface. The lock-in amplifier (Moku:Lab) and data acquisition card measured the time-resolved photocurrent and voltage signals passing through the envelope detector. At the same time, the field-programmable gate array (FPGA) collected the phase detector output as the relaxation time signal and synchronously controlled the voltage scan of the high-voltage power supply and the chopper frequency. The incident light source came from white-light lasers (SuperK COMPACT) and two cascaded variable bandwidth single-line tunable filters (SuperK LLTF Contrast, tunable wavelength range 400–1,000 nm, wavelength resolution <0.32 nm) to control the wavelength and a programmable optical attenuator to control the light intensity. Before testing, the photomultiplier tube was used to calibrate the base attenuation intensity at different wavelengths to ensure that the power density of the emitted light was equal. Cascaded monochromators were assembled to obtain narrower monochromatic light. Polychromatic light was introduced through a beam-splitting system with multiple monochrome lasers.

Spectral reconstruction method

Our machine learning model was implemented by using Keras. The photocurrent and relaxation signals were concatenated and fed into a DNN of five hidden layers. The input vectors were first normalized to the standard normal distribution and simultaneously generated corresponding means and variances, which were added to the initial vectors. Then, the data stream passed through hidden layers with sigmoid activation functions and, finally, reconstructed intensities were predicted at each preinstalled wavelength in the output layer. DNN training was done by adaptive moment estimation on the mean-squared error for training epochs with a mini-batch size of 32. The learning rate was optimized dynamically by adopting warmup and cosine annealing strategies. Ten-fold cross-validation and Gaussian noise disturbance were used to prevent overfitting during training. The test set of unseen data was used to estimate the reconstructive performance including the generalization error.

Data availability

The data that support the findings of this study are available via Zenodo at https://doi.org/10.5281/zenodo.10052205 (ref. 33). Other data are available from the corresponding author upon reasonable request.

Code availability

The custom code used for dual-signal spectral reconstruction is available at https://github.com/iCalculate/Dual-spectral-reconstruction.

References

1. Yang, Z., Albrow-Owen, T., Cai, W. & Hasan, T. Miniaturization of optical spectrometers. *Science* **371**, eabe0722 (2021).
2. Grotevent, M. et al. Integrated photodetectors for compact Fourier-transform waveguide spectrometers. *Nat. Photonics* **17**, 59–64 (2023).
3. Tittl, A. et al. Imaging-based molecular barcoding with pixelated dielectric metasurfaces. *Science* **360**, 1105–1109 (2018).
4. Zhou, J., Chizhik, A. I., Chu, S. & Jin, D. Single-particle spectroscopy for functional nanomaterials. *Nature* **579**, 41–50 (2020).
5. Li, A. & Fainman, Y. On-chip spectrometers using stratified waveguide filters. *Nat. Commun.* **12**, 2704 (2021).
6. Cai, G. et al. Compact angle-resolved metasurface spectrometer. *Nat. Mater*. https://doi.org/10.1038/s41563-023-01710-1 (2023).
7. Cheng, R. et al. Broadband on-chip single-photon spectrometer. *Nat. Commun.* **10**, 4104 (2019).
8. Deng, W. et al. Electrically tunable two-dimensional heterojunctions for miniaturized near-infrared spectrometers. *Nat. Commun.* **13**, 4627 (2022).
9. Martinez, A. Tiny spectrometers. *Nat. Mater.* **22**, 947 (2023).
10. Long, D. et al. Nanosecond time-resolved dual-comb absorption spectroscopy. *Nat. Photonics* https://doi.org/10.1038/s41566-023-01316-8 (2023).
11. Pohl, D. et al. An integrated broadband spectrometer on thin-film lithium niobate. *Nat. Photonics* **14**, 24–29 (2020).
12. Bao, J. & Bawendi, M. G. A colloidal quantum dot spectrometer. *Nature* **523**, 67–70 (2015).
13. Huang, E., Ma, Q. & Liu, Z. Etalon array reconstructive spectrometry. *Sci. Rep.* **7**, 40693 (2017).
14. Wang, Z. et al. Single-shot on-chip spectral sensors based on photonic crystal slabs. *Nat. Commun.* **10**, 1020 (2019).
15. Yang, Z. et al. Single-nanowire spectrometers. *Science* **365**, 1017–1020 (2019).
16. Yuan, S., Naveh, D., Watanabe, K., Taniguchi, T. & Xia, F. A wavelength-scale black phosphorus spectrometer. *Nat. Photonics* **15**, 601–607 (2021).
17. Yoon, H. H. et al. Miniaturized spectrometers with a tunable van der Waals junction. *Science* **378**, 296–299 (2022).
18. Li, F. et al. Recent advances in strain-induced piezoelectric and piezoresistive effect-engineered 2D semiconductors for adaptive electronics and optoelectronics. *Nanomicro. Lett.* **12**, 106 (2020).
19. Wu, W. et al. Piezoelectricity of single-atomic-layer MoS_2 for energy conversion and piezotronics. *Nature* **514**, 470–474 (2014).
20. Zhu, H. et al. Observation of piezoelectricity in free-standing monolayer MoS_2. *Nat. Nanotechnol.* **10**, 151–155 (2015).
21. Scopel, W. L., Miwa, R. H., Schmidt, T. M. & Venezuela, P. MoS_2 on an amorphous HfO_2 surface: an ab initio investigation. *J. Appl. Phys.* **117**, 194303 (2015).
22. Li, Z. et al. Efficient strain modulation of 2D materials via polymer encapsulation. *Nat. Commun.* **11**, 1151 (2020).
23. Gant, P. et al. A strain tunable single-layer MoS_2 photodetector. *Mater. Today* **27**, 8–13 (2019).
24. Xu, H. et al. Spatially bandgap-graded $MoS_{2(1-x)}Se_2x$ homojunctions for self-powered visible-near-infrared phototransistors. *Nanomicro. Lett.* **12**, 26 (2020).
25. Jiang, J. et al. Flexo-photovoltaic effect in MoS_2. *Nat. Nanotechnol.* **16**, 894–901 (2021).
26. Herberholz, R. et al. Distinction between bulk and interface states in $CuInSe_2$/CdS/ZnO by space charge spectroscopy. *J. Appl. Phys.* **83**, 318–325 (1998).
27. Zhang, J., Zhu, X. & Bao, J. Denoising autoencoder aided spectrum reconstruction for colloidal quantum dot spectrometers. *IEEE Sens. J.* **21**, 6450–6458 (2021).
28. Pi, L. et al. Broadband convolutional processing using band-alignment-tunable heterostructures. *Nat. Electron.* **5**, 248–254 (2022).
29. Guo, L. et al. A single-dot perovskite spectrometer. *Adv. Mater.* **34**, 2200221 (2022).
30. Sun, H. et al. In situ formed gradient bandgap-tunable Perovskite for ultrahigh-speed color/spectrum-sensitive photodetectors via electron-donor control. *Adv. Mater.* **32**, 1908108 (2020).
31. Kurokawa, U., Choi, B. I. & Chang, C.-C. Filter-based miniature spectrometers: spectrum reconstruction using adaptive regularization. *IEEE Sens. J.* **11**, 1556–1563 (2011).
32. Gao, L., Qu, Y., Wang, L. & Yu, Z. Computational spectrometers enabled by nanophotonics and deep learning. *Nanophotonics* **11**, 2507–2529 (2022).
33. Du, X. Dual spectral reconstruction for nm-resolution microspectrometers. *Zenodo* https://doi.org/10.5281/zenodo.10052205 (2023).

Acknowledgements

We thank T. C. Zhou and A. J. Zhou from the Analysis and Testing Center, University of Electronic Science and Technology of China, for the technical support with scanning electron microscopy and Raman imaging. We thank Z. Wang, Y. Yang, D. Xu, S. Deng, X. Wang, P. Li and C. Yang for the constructive discussions. This work was supported by the National Key Research and Development Program of China (reference no. 2021YFA0718800 to J.X.), the National Natural Science Foundation of China (reference no. 52372177 to Y.Z.) and Young Scientists Fund of the National Natural Science Foundation of China (reference no. 52001059 to C.W.).

Author contributions

X.D. and Y.Z. formulated and directed the research. J.X. supervised the project. X.D. designed and fabricated devices with the assistance of J.H., X.C. and T.Z. X.D. and Y.W. conducted optoelectronic performance characteristic. G.R. and C.W. performed the physical characterization. Y.Z. and X.D. analysed data and provided theoretical explanations. X.D. and Y.C. developed the restructured algorithm and code. T.Z., Y.C. and J.H. provided substantial assistance in practical application demonstrations. X.D. wrote the paper under the direction of Y.Z., H.C., Z.Y. and J.X. All authors participated extensively in scientific discourse, commented on the experimental results and made substantive contributions to the paper.

Competing interests

The authors declare no competing interests.

Additional information

Supplementary information The online version contains supplementary material available at https://doi.org/10.1038/s41928-024-01242-9.

Correspondence and requests for materials should be addressed to Hanxiao Cui or Yicheng Zhao.

Peer review information *Nature Electronics* thanks Yuan Li and Qinghai Song for their contribution to the peer review of this work.